Elliptical Lunar Frozen Orbit Constellation Design within a Model of Evolving Fidelity

Conference Paper · January 2025

CITATIONS
0

READS
94

3 authors, including:

Beom Park
Purdue University West Lafayette
16 PUBLICATIONS **88** CITATIONS
SEE PROFILE

Kathleen Howell
Purdue University West Lafayette
337 PUBLICATIONS **7,949** CITATIONS
SEE PROFILE

AAS 25-165

ELLIPTICAL LUNAR FROZEN ORBIT CONSTELLATION DESIGN WITHIN A MODEL OF EVOLVING FIDELITY

Beom Park*, Kathleen C. Howell†, Shaun Stewart‡

Satellite constellations in Elliptical Lunar Frozen Orbits (ELFOs) are suitable for supporting various missions in the lunar vicinity. Although these orbits exhibit stable behavior under idealized averaged dynamics, higher-fidelity modeling and mission requirements that include maintaining relative phasing within the constellation, pose unique challenges. This investigation explores strategies for rapidly refining ELFOs within a high-fidelity ephemeris model, significant for constellation design. The approach leverages a dense quasi-periodic orbit solution space and a frequency domain targeting method to address these challenges.

INTRODUCTION

Elliptical Lunar Frozen Orbits (ELFOs) offer an attractive option to support various missions in the lunar vicinity. These orbital structures supply near-stability over a long horizon time and the ability to provide extended line-of-sight to the Lunar South Pole (LSP), a key region for expanding cislunar space activities in the near future [1]. Leveraging these benefits, multiple space entities envision the inclusion of one or more satellites in ELFOs[1][2] as a part of a data relay system. The ELFOs satisfy the "frozen" condition, admitting nearly constant *mean* eccentricity, inclination, and argument of perilune [2]. While a variety of orbits supply such a condition, the ELFOs are characterized by relatively high altitude, inclination and eccentricity values, where the point-mass Earth gravity significantly contributes to the stable evolution of the orbit geometry [3].

While ELFOs exist in the vicinity of the equilibria derived from simplified, doubly-averaged dynamical models [2–5], the trajectories must be *refined* within a higher-fidelity model such that they are suitable for actual flight. Two broad approaches in the literature address this refinement: (i) semi-analytical and (ii) fully-numerical methods. The first strategy locates a closed-form transformation between the *mean* orbital elements and the *osculating* orbital elements; while the frozen, equilibria conditions are derived in terms of the former, the actual mission analysis requires the representation of the initial condition in the latter, suitable for accurate numerical propagations. While the circular Earth-Moon motion and lunar harmonics of lower degree are assumed in the literature [2] to describe the transformation, a knowledge gap exists in deriving the semi-analytical relationship in the presence of the realistic Earth-Moon motion, thus, still necessitating further numerical strategies. The second

*Ph.D. Candidate, School of Aeronautics and Astronautics, Purdue University, West Lafayette, IN 47907
†Hsu Lo Distinguished Professor, School of Aeronautics and Astronautics, Purdue University, West Lafayette, IN 47907
‡Flight Dynamics Lead, Intuitive Machines, 13467 Columbia Shuttle Street, Houston, TX 77059

[1] https://www.intuitivemachines.com/post/nasa-selects-intuitive-machines-to-deliver-4-lunar-payloads-in-2024, Accessed: 09-05-2024

[2] https://spacenews.com/china-could-develop-dual-relay-satellite-system-for-earth-moon-communications-to-reduce-geopolitical-risks, Accessed: 09-05-2024

strategy, i.e., the fully-numerical approach, typically employs a differential corrector to refine the ELFOs directly within the complex dynamics. While multiple examples appear in the literature that adopt models with varying fidelities [6, 7], a systematic corrections process remains elusive to refine ELFOs within a higher-fidelity model.

For designing and operating a satellite *constellation* within ELFOs, the capabilities to rapidly refine ELFOs within a higher-fidelity model are increasingly important. Such capabilities aid in exploration of the trade space for nominal transfer costs, including maneuvers and time-of-flight, to achieve various constellations under specific mission requirements. Additionally, the constellation introduces phase constraints between satellites, necessitating precise initial states to maintain these constraints throughout the mission timeline. Various stochastic errors, such as navigation inaccuracies, may arise during operations, potentially requiring reconfiguration of the entire constellation. In such scenarios, the ability to quickly refine ELFO trajectories is critical for efficiently characterizing alternative solutions.

This investigation proposes a methodology for rapidly refining ELFOs within higher-fidelity models, facilitating the design and analysis of satellite constellations. The approach involves characterizing the quasi-periodic solution space surrounding ELFOs using numerical algorithms across varying fidelity levels. A new differential corrections technique, termed the "frequency domain targeter," is introduced to exploit these dense quasi-periodic structures in higher-fidelity models. The effectiveness of the proposed methodology is demonstrated through a sample ELFO constellation of three satellites focused on the Lunar South Pole (LSP).

PRELIMINARIES

This section introduces the foundational concepts essential for the analysis in subsequent sections. Different reference frames and their associated state transformations serve as the basis along with dynamical models reflecting varying fidelity levels. Lastly, numerical algorithms for characterizing quasi-periodic structures in the ELFO solution space are reviewed.

Frames and Transformations

Three different frames are employed in the current work. These various frames facilitate analyses of ELFOs across models with varying fidelity levels as follows:

(Frame 1) Barycentric Rotating Frame (BRF): this frame adopts an orthogonal basis $\hat{x} - \hat{y} - \hat{z}$ defined as, (1) $\hat{x}$ directs from the Earth to the Moon, (2) $\hat{z}$ coincides with the angular momentum of the Moon with respect to Earth, and (3) $\hat{y}$ completes the dextral triad. The origin of the frame is located at the Earth-Moon barycenter. With the Earth-Moon distance normalized to be unity (regardless of the actual dimensional distance), this frame renders fixed locations for the Earth and Moon on the $\hat{x}$ axis at $-\mu$ and $(1-\mu)$. The mass ratio μ measures the ratio of the mass of the Moon with respect to the Earth-Moon system mass. The nondimensional (nd) spacecraft position vector is expressed as $\vec{\rho} = x\hat{x} + y\hat{y} + z\hat{z}$.

(Frame 2) Moon-Centered Earth Orbit Frame (EOF): the orthonormal basis $\hat{X}_E - \hat{Y}_E - \hat{Z}_E$ is constructed such that $\hat{Z}$ coincides with $\hat{z}$, and $\hat{X} - \hat{Y}$ are produced by rotating $\hat{x} - \hat{y}$ at a constant negative rate with respect to $\hat{Z}$. The origin of the frame is located at the center of the Moon. The nd spacecraft position vector within the EOF is then constructed as,

$$\vec{R}_E = \boldsymbol{C}_E(\vec{\rho} - \vec{\rho}_M) = X_E\hat{X}_E + Y_E\hat{Y}_E + Z_E\hat{Z}_E, \quad \boldsymbol{C}_E = \begin{bmatrix} \cos(t+t_0) & -\sin(t+t_0) & 0 \\ \sin(t+t_0) & \cos(t+t_0) & 0 \\ 0 & 0 & 1 \end{bmatrix}, \tag{1}$$

where $\rho_M = (1-\mu)\hat{x}$, the nd lunar position vector within the BRF. The nd time t is constructed leveraging the characteristic quantities l_* and t_* defined as the average Earth-Moon distance and $t_* = \sqrt{l^*/(\tilde{\mu}_E + \tilde{\mu}_M)}$ where $\tilde{\mu}_{E,M}$ are the dimensional gravitational parameters for the Earth and Moon, respectively. Then, t normalizes the dimensional time via t_*. The initial epoch t_0 determines the configuration of the Earth-Moon system within the EOF. This frame is defined consistent with previous investigations [3, 4, 8]. For the nd position and velocity, i.e., $\vec{R}_E, \vec{R}'_E = d\vec{R}_E/dt$, the osculating orbital elements œ with respect to the Moon are retrieved leveraging standard transformation schemes, e.g., in Vallado [9], i.e., œ $=$ œ$(\vec{R}_E, \vec{R}'_E)$. The classical Keplerian elements are adopted in the current investigation as follows: a (semi-major axis), e (eccentricity), i (inclination), ω (argument of perilune), Ω (right ascension of the ascending node), and M (mean anomaly). To facilitate analysis for the ELFOs, it is common practice to *average* the perturbations from the Earth along the lunar orbit with respect to both M and Ω. This process results in the *doubly-averaged* mean orbital elements, $\bar{\bar{\text{œ}}}$, where the double bar indicates the quantity is averaged twice.

(Frame 3) Moon-Centered J2000 Inertial Frame (JIF): the unit vectors $\hat{X} - \hat{Y} - \hat{Z}$ are defined consistent with the J2000 inertial frame. The nd spacecraft position vector in the frame is rendered as,

$$\vec{R} = \frac{l}{l_*}\boldsymbol{C}(\vec{\rho} - \vec{\rho}_M) = X\hat{X} + Y\hat{Y} + Z\hat{Z}, \quad \boldsymbol{C} = \begin{bmatrix} \hat{x} & \hat{y} & \hat{z} \end{bmatrix}, \tag{2}$$

where l, l_* are the instantaneous and mean Earth-Moon distances, respectively. The unit vectors $\hat{x} - \hat{y} - \hat{z}$ are constructed instantaneously based on the numerical ephemerides DE440 [10]. Building upon these frames, the transformations between the various state representations are summarized in Fig. 1. The transformation between doubly-averaged mean elements, $\bar{\bar{\text{œ}}}$, and osculating elements, œ, is a non-trivial process in general, where a suitable transformation depends on the instantaneous configurations in the system. In the current investigation, however, $\bar{\bar{\text{œ}}} =$ œ, i.e., both elements are treated equivalently. Such an approximation is justified from the fact that any semi-analytical transformation between $\bar{\bar{\text{œ}}}$ and œ still requires further refinement. This work focuses on the refinement algorithm itself, alleviating the dependency on an accurate transformation between $\bar{\bar{\text{œ}}}$ and œ. The rest of the transformations in Fig. 1 are provided more trivially via Eqs. (1)-(2). Note that the velocities, i.e., $\vec{R}'_E, \vec{\rho}', \vec{R}'$, are connected via derivatives for these equations.

Fig. 1: Transformations across various state representations and frames

Dynamical Models

Three different dynamical models are reviewed, focusing on their various degrees of fidelity. Doubly-Averaged Dynamical Model (DADM), Circular Restricted Three-Body Problem (CR3BP),

and Higher-Fidelity Ephemeris Model (HFEM) serve as lower-, medium-, and higher-fidelity models in description of the ELFOs and their nearby dynamical structures.

Doubly-Averaged Dynamical Model (DADM) Within the Moon-dominated dynamical regime, several assumptions are introduced to supply the DADM employed in the current investigation. Firstly, the point-mass Earth is the only perturbing body. While it is possible to extend the DADM to include the perturbations from the nonspherical gravity from the Moon [2], such extensions are not considered here as the focus remains on the ELFOs where the most dominant perturbations originate from the Earth [3]. Then, the Earth's perturbing potential is truncated leveraging the Legendre expansion as detailed by Longuski et al. [11]. Subsequently, the perturbation from the Earth is averaged over (1) Ω and (2) M to supply the doubly-averaged, truncated Earth perturbing potential,

$$\bar{\bar{P}} = \frac{1}{32} n_E \bar{\bar{a}}^2 \left[(1 + 3\cos 2\bar{\bar{i}})(2 + 3\bar{\bar{e}}^2) + 30\bar{\bar{e}}^2 \sin^2 \bar{\bar{i}} \cos 2\bar{\bar{\omega}} \right]. \tag{3}$$

where n_E is the dimensional mean angular rate for the Earth around the Moon. Recall that the doubly-averaged mean elements, i.e., $\bar{\bar{\mathfrak{E}}}$, are supplied within the EOF. From Lagrange's planetary equations, the mean orbital elements evolve at the following rates,

$$\frac{d\bar{\bar{a}}}{dt} = 0 \tag{4}$$

$$\frac{d\bar{\bar{e}}}{dt} = \frac{15}{8} \frac{(1-\mu) n_E^2}{\bar{\bar{n}} t_*} \bar{\bar{e}} (1 - \bar{\bar{e}}^2)^{1/2} \sin^2 \bar{\bar{i}} \sin 2\bar{\bar{\omega}} \tag{5}$$

$$\frac{d\bar{\bar{i}}}{dt} = -\frac{15}{16} \frac{(1-\mu) n_E^2}{\bar{\bar{n}} t_*} \frac{\bar{\bar{e}}^2}{(1 - \bar{\bar{e}}^2)^{1/2}} \sin 2\bar{\bar{i}} \sin 2\omega \tag{6}$$

$$\frac{d\bar{\bar{\omega}}}{dt} = \frac{3}{16} \frac{(1-\mu) n_E^2}{\bar{\bar{n}} t_*} \frac{1}{(1 - \bar{\bar{e}}^2)^{1/2}} \left[(3 + 2\bar{\bar{e}}^2 + 5\cos 2\bar{\bar{i}}) + 5(1 - 2\bar{\bar{e}}^2 - \cos 2\bar{\bar{i}}) \cos 2\bar{\bar{\omega}} \right] \tag{7}$$

$$\frac{d\bar{\bar{\Omega}}}{dt} = \frac{3}{8} \frac{(1-\mu) n_E^2}{\bar{\bar{n}} t_*} \frac{1}{(1 - \bar{\bar{e}}^2)^{1/2}} (5\bar{\bar{e}}^2 \cos 2\bar{\bar{\omega}} - 3\bar{\bar{e}}^2 - 2) \cos \bar{\bar{i}} \tag{8}$$

$$\frac{d\bar{\bar{M}}}{dt} = -\frac{1}{8} \frac{(1-\mu) n_E^2}{\bar{\bar{n}} t_*} \frac{1}{(1 - \bar{\bar{e}}^2)^{1/2}} \left[(3\bar{\bar{e}}^2 + 7)(3\cos^2 \bar{\bar{i}} - 1) + 15(1 + \bar{\bar{e}}^2) \sin^2 \bar{\bar{i}} \cos^2 \bar{\bar{\omega}} \right], \tag{9}$$

where $\bar{\bar{n}}$ is the dimensional mean motion for the satellite around the Moon supplied with $\bar{\bar{a}}$.

Circular Restricted Three-Body Problem (CR3BP) The CR3BP dynamics are cast within the BRF. The equations of motion are rendered as,

$$\vec{\rho}'' = -2\hat{z} \times \vec{\rho}' + \nabla V. \tag{10}$$

The double prime indicates a second derivative with respect to the nd time, t. The vector cross product is denoted as $\times$, and V is the pseudo-potential function rendered as $V = 1/2 \cdot (x^2 + y^2) + (1-\mu)/d + \mu/r$ where d and r correspond to the nd distance between the spacecraft and Earth, and the spacecraft and Moon, respectively. Note that the CR3BP serves as a "medium-fidelity" model bridging the DADM and HFEM via relaxing two key simplifying assumptions: (1) truncated Earth potential and (2) doubly-averaging process. Removing only the latter assumption results in the Hill Restricted Three-Body Problem (HR3BP) that also serves as a suitable intermediate model [12]. The current work adopts the CR3BP to simultaneously assess the impact from both simplifying assumptions.

Higher-Fidelity Ephemeris Model (HFEM) The higher-fidelity modeling in the current investigation includes points-mass gravity from three celestial bodies: the Sun (S), Earth (E), and Moon (M). The instantneuos locations of the bodies are retrieved from the JPL ephemerides DE440 [10]. With the Moon as the central gravitational body, the equations of motion for the spacecraft within the JIF are rendered,

$$\vec{R}'' = -\frac{\mu}{R^3}\vec{R} + \sum_{j=E,S}\left[\frac{\mu_j}{R_{jM}^3}\vec{R}_{jM} - \frac{\mu_j}{R_{jc}^3}\vec{R}_{jc}\right], \tag{11}$$

where $\vec{R}_{jc}$ and $\vec{R}_{jM}$ denote the nd position vectors from the perturbing body j to the spacecraft and the Moon, respectively. The nd gravitational parameter μ_j is defined as $\mu_j = \tilde{\mu}_j/(\tilde{\mu}_E + \tilde{\mu}_M)$. Subscripts E, S are leveraged to indicate the Earth and the Sun, respectively.

Quasi-Periodic Orbit Computation Algorithm [13, 14]

The ELFOs and nearby structures in various dynamical models are often characterized as quasi-periodic orbits, i.e., invariant tori. In the current work, these quasi-periodic orbits are approximately constructed via an algorithm introduced by Gómez and Mondelo [13] as well as Olikara and Scheeres [14] (GMOS). The focus is specifically on two-dimensional (2D) and three-dimensional (3D) tori. The GMOS algorithm employs a stroboscopic map synchronized to the period of one of the tori's fundamental frequencies. This approach reduces the dimensionality of the problem, enabling one-dimensional (1D) invariant curves and 2D invariant surfaces to emerge in the map for 2D and 3D tori, respectively. Each time the state revisits the stroboscopic map, it rotates by fixed angles, termed rotation numbers (σ), along these invariant structures. To approximate the structures, the GMOS algorithm employs discrete Fourier series with finite sample points, and the invariance condition is enforced using differential correctors. For the 2D tori case, the invariant curve at the map is expressed as,

$$\vec{u}(\theta) \approx \exp(\mathrm{i}\vec{m}\theta)\boldsymbol{A}, \tag{12}$$

where $\mathrm{i}^2 = -1$ and exp is the exponential function. The invariant curve $\vec{u}$ is a six-dimensional row vector parameterized by one angle, θ, and $\boldsymbol{A}$ denotes the Fourier coefficient matrix of size $(N_F, 6)$ with N_F samples to approximate the Fourier series. The index vector $\vec{m}$ is rendered as

$$\vec{m} = \begin{bmatrix} -(N_F-1)/2 & -(N_F-1)/2+1 & \ldots & (N_F-1)/2-1 & (N_F-1)/2 \end{bmatrix}. \tag{13}$$

Then, the invariance condition is formulated as,

$$\vec{\Psi}(\vec{u}(\theta)) - \vec{u}(\theta+\sigma) = \vec{0}, \tag{14}$$

where $\vec{\Psi}$ represents the stroboscopic flow map for a given dynamical model. To approximate the invariant curve from Eq. (12), N_F state vectors are sampled, and the invariance condition in Eq. (14) is enforced as $6N_F$ scalar constraints. Consequently, the $6N_F$ state components are adjusted through differential corrections to satisfy these constraints. The Jacobian matrix $\boldsymbol{DF}$, of size $(6N_F, 6N_F)$, captures the sensitivity of the invariance condition to variations in the states along the invariant curve. It serves a role analogous to the monodromy matrix used for periodic orbits, but within the context of 2D tori [15]. For brevity, the mathematical formulation for the computation of 3D tori is omitted in this work. For detailed discussions, refer to prior studies [16, 17].

Frequency Collocation Algorithm [18]

As the ELFOs are often characterized as quasi-periodic orbits, it is crucial to analyze their underlying frequency structures and those of nearby trajectories. The Fourier-transformed data for these trajectories reveal frequencies represented as integer linear combinations of a finite number of fundamental frequencies. Due to the absence of closed-form solutions for such trajectories, the Discrete Fourier Transform (DFT) is employed to extract frequency-domain information. However, this method faces several challenges. Due to the discrete nature of the method, a limit on the frequency resolution exists. Spectral leakage occurs where any true peak in the signal "leaks" to multiple peaks. For illustration, consider the DFT on the x position of an arbitrary quasi-periodic trajectory (Γ) constructed as,

$$\mathcal{X}_\Gamma(k) = \frac{1}{N}\sum_{j=0}^{N-1} x_\Gamma(t_j)h(j)\exp(-2\pi \mathrm{i} jk/N), \quad (k = 0, 1, 2, ..., N-1), \tag{15}$$

where t_j is the j-th sample time constructed as $t_j = j\Delta t$ with equally spaced time Δt between the samples and $0 \leq j \leq N-1$. The Hann window smoothing function of order 2 is supplied as $h(j) = 2/3\,[1-\cos(2\pi j/(N-1))]^2$, a typical process to reduce the spectral leakage [18, 19]. The peak frequency index k is identified when $\mathcal{X}_\Gamma(k) > \mathcal{X}_\Gamma(k \pm 1)$. The true frequency of the quasi-periodic trajectory, however, typically does not coincide at $\nu_k = 2\pi k/t_{N-1}$ due to the discrete nature of the strategy. Note that the resolution of the detected frequency is limited at $2\pi/t_{N-1}$, governed by the total span of the time for the signal, t_{N-1}.

To address the inherent challenges of the DFT, Gómez et al. [18] introduce a collocation algorithm to refine frequency-domain information. The algorithm uses algebraic relationships to construct more accurate estimates of amplitude A_i, frequency ν_i, and phase angle θ_i for each detected i-th DFT peak. The principle is that the frequency response from the DFT must align with that of a reconstructed signal $A_i\cos(\nu_i t + \theta_i)$. To solve for the unknown variables A_i, ν_i, θ_i, the following square linear system of equations is constructed,

$$A_i\cos\theta_i c_{c(\nu_i)}(k) - A_i\sin\theta_i c_{s(\nu_i)}(k) = c_\Gamma(k), \tag{16}$$

$$A_i\cos\theta_i s_{c(\nu_i)}(k) - A_i\sin\theta_i s_{s(\nu_i)}(k) = s_\Gamma(k), \tag{17}$$

$$A_i\cos\theta_i cs_{c(\nu_i)}(k\pm 1) - A_i\sin\theta_i cs_{s(\nu_i)}(k\pm 1) = cs_\Gamma(k\pm 1), \tag{18}$$

where k is the detected index of the peak from the DFT. It is assumed that a true peak exists between the k and $(k \pm 1)$. The sign for $\pm$ is determined based on the larger norm for $\mathcal{X}_\Gamma(k \pm 1)$. The right sides of Eqs. (16)-(17) are constructed as,

$$c_\Gamma(k) = 2\,\mathrm{Re}\left(\mathcal{X}_\Gamma(k)\right), \quad s_\Gamma(k) = -2\,\mathrm{Im}\left(\mathcal{X}_\Gamma(k)\right), \tag{19}$$

connected to the real (cosine) and imaginary (sine) components of Eq. (15). On the left side of Eqs. (16)-(17), $c(\nu_i) = \cos(\nu_i t)$ and $s(\nu_i) = \sin(\nu_k t)$, and,

$$\begin{aligned} c_{c(\nu_i)}(k) &= 2\,\mathrm{Re}\left(\mathcal{X}_{c(\nu_i)}(k)\right), \quad c_{s(\nu)}(k) = 2\,\mathrm{Re}\left(\mathcal{X}_{s(\nu_i)}(k)\right), \\ s_{c(\nu)}(k) &= -2\,\mathrm{Im}\left(\mathcal{X}_{c(\nu_i)}(k)\right), \quad s_{s(\nu_i)}(k) = -2\,\mathrm{Im}\left(\mathcal{X}_{s(\nu_i)}(k)\right), \end{aligned} \tag{20}$$

corresponding to the DFT response for the cosine and sine functions with the frequency ν_i. In Eq. (18), the expression cs is selected as either c or s that ensures an invertible system of linear equations utilizing a criterion provided in Gómez et al. [18, 20]. For the i-th peak detected in DFT, Eqs. (16)-(18) iteratively refine A_i, ν_i, θ_i. The process is repeated for subsequent peaks, gradually building a set of refined frequency parameters for the quasi-periodic trajectory Γ.

ELLIPTICAL LUNAR FROZEN ORBITS AND NEARBY STRUCTURES: DENSE SOLUTION SPACE

To effectively design constellations leveraging ELFOs, it is essential to understand the characteristics of the solution space within a realistic dynamical model. This process requires a comprehensive analysis of ELFOs and their surrounding structures, considering *dense* quasi-periodic orbits across models with varying levels of fidelity.

Review: ELFOs in the Doubly-Averaged Dynamical Model (DADM)

Initially, the solution space within the lower-fidelity model, i.e., DADM, is reviewed. From Eqs. (4)-(9), three integrals of motion exist [8] as follows,

$$C_Z = (1 - \bar{\bar{e}}^2)\cos^2\bar{\bar{i}} \tag{21}$$

$$C_H = \bar{\bar{e}}^2(2/5 - \sin^2\bar{\bar{i}}\sin^2\bar{\omega}) \tag{22}$$

$$C_a = \bar{\bar{a}}, \tag{23}$$

related to the out-of-plane angular momentum, total energy, and the semi-major axis, respectively. With these three independent integrals of motion, given the three degree-of-freedom Hamiltonian dynamics (available in Nie and Gurfil [2]), the DADM is completely integrable in the sense of Liouville-Arnold [21]. Consequently, any initial condition within the DADM is perpetually bounded on invariant tori, ensuring stability [22].

The integrable nature of the DADM is also apparent from Eqs. (4)-(9). Examine that the right sides of the equations solely consist of $\bar{\bar{e}}, \bar{\bar{i}}, \bar{\omega}$. With the separable dynamics for $\bar{\bar{e}}, \bar{\bar{i}}, \bar{\omega}$, the first two integrals of motion from Eqs. (21)-(22) are functions of these three variables. Thus, these three variables always trace either fixed points or periodic orbits. This behavior is visualized in Fig. 2. Two integrals of motion, C_Z, C_H, are plotted on the horizontal and vertical axes of Fig. 2(a). Solutions exist on and within the black boundaries. Two fundamental behaviors are observed for $C_H > 0$ and $C_H < 0$. For $C_H > 0$, the argument of perilune $\bar{\omega}$ completes full revolutions, corresponding to *circulating* orbits. For $C_H < 0$, $\bar{\omega}$ *librates* in the vicinity of $90°, 270°$. This behavior is separated by $C_H = 0$, corresponding to a fixed point (indicated by the cyan line). The lower bound for C_H is marked by the magenta line that corresponds to the ELFOs satisfying following equilibrium conditions,

$$\bar{\omega}_{eq} = 90°, 270° \tag{24}$$

$$\bar{\bar{e}}_{eq} = \sqrt{1 - 5/3\cos^2\bar{\bar{i}}_{eq}}. \tag{25}$$

Note that the ELFOs exist only when $C_Z \leq 3/5$. The gray region within Fig. 2(a) denotes the "nearby" solutions for the ELFOs. The current investigation focuses on the ELFOs (magenta line) and the nearby structures (gray surface). For a sample value of C_Z, corresponding orbits within the $\bar{\bar{e}} - \bar{\omega}$ space are illustrated in Fig. 2(b). The cyan star (★) denotes the fixed point at $C_H = 0$. The magenta star (★) is the ELFO, and surrounding nearby structures are illustrated with different colors and exist as periodic orbits within the $\bar{\bar{e}} - \bar{\omega}$ space[3]. The inclination, $\bar{\bar{i}}$, is trivially decided from C_Z, C_H, and not explicitly plotted. In summary, within the $\bar{\bar{e}}, \bar{\omega}, \bar{\bar{i}}$ space, the ELFOs and nearby structures track fixed points and periodic orbits. Within the full six-dimensional space ($\bar{\bar{\text{œ}}}$), these

[3]Two magenta stars appear in Fig. 2(b) that correspond to the northern and southern orbits associated with $\bar{\omega} = 270°$ and $90°$, respectively.

structures generally track 2D and 3D tori, respectively. Observe that the frequencies for $\bar{\bar{\Omega}}$ and $\bar{\bar{M}}$ in Eqs. (8)-(9) are distinct from the frequency of the periodic orbits within the $\bar{\bar{e}}, \bar{\bar{\omega}}, \bar{\bar{i}}$ space. In general, these three frequencies are incommensurate and, thus, the ELFOs and nearby structures exist as 2D and 3D tori within the DADM. Recall that the semi-major axis $\bar{\bar{a}}$ remains constant within the DADM and serves as the third integral of motion. Thus, the ELFOs and nearby structures track two- and three-parameter families as depicted in Fig. 2(c). With C_a serving as the new dimension, the 2D surface from Fig. 2(a) extends to the 3D volume. Here, the ELFOs exist on the 2D magenta surface and the nearby structures within the 3D gray volume.

The three-frequencies that constitute the ELFOs and surrounding structures are categorized in terms of their respective periods. The short-period corresponds to one complete revolution for $\bar{\bar{M}}$, that depends on $\bar{\bar{a}}$, and is on the order of a day. The medium-period is associated with the passage of 2π [radians] for the modified right ascension defined as $\bar{\bar{\Omega}}_M = t - \bar{\bar{\Omega}}$ as measured within the BRF. Noting that $d\bar{\bar{\Omega}}/dt < 0$ for $\bar{\bar{\omega}} = 90^\circ$ and $\bar{\bar{i}} \leq 90^\circ$ (Eq. (8)), the period for $\bar{\bar{\Omega}}_M$ is slightly larger than 2π, on the order of a month. Lastly, the long-period pertains to the orbits as tracked within the $\bar{\bar{e}} - \bar{\bar{\omega}}$ space. While specific values differ by the combinations of $\bar{\bar{e}} - \bar{\bar{i}} - \bar{\bar{\omega}}$, it is generally associated with periods on the order of a year. These periods are denoted as short-, medium-, and long-periods in the current analysis. The nd frequencies associated with the periods are denoted as $\nu_{S,M,L}$, respectively.

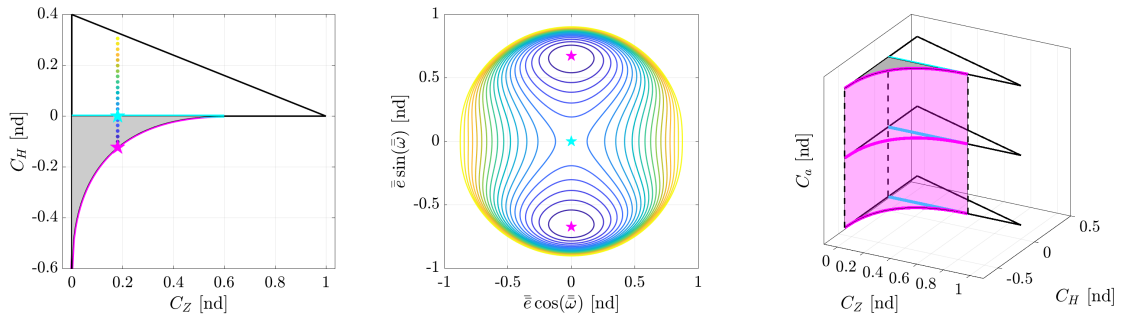

(a) 2D Surface Constants in DADM (b) $\bar{\bar{e}} - \bar{\bar{\omega}}$ space (c) 3D Surface Constants in DADM

Fig. 2: Solution space visualization for the DADM

ELFOs in the Circular Restricted Three-Body Problem (CR3BP)

The CR3BP is not an integrable system and, thus, it is nontrivial to characterize the evolution of the DADM solution space within the CR3BP. While it is possible to demonstrate the persistence of tori with Kolmogorov-Arnold-Moser (KAM) techniques [22], the current investigation remains primarily numerical. The tori within the CR3BP are directly approximated with the GMOS algorithm, alluding to the persistence of the invariant tori. Starting with ELFOs from the DADM, 2D tori are constructed within the CR3BP, providing the basis for generating and converging initial guesses for 3D tori. This approach offers insights into the nature of the evolving ELFO solution space across multiple models, as well as intuition about the geometry and frequencies of ELFOs manifesting in different frames.

2D Tori The 2D tori from the DADM potentially persist as 2D tori within the CR3BP dynamics. For computation of 2D tori with the GMOS algorithm, the stroboscopic map is constructed with the period of one of the two frequencies, $\nu_{S,M}$. Note that the oscillations in the third frequency, ν_L, do not exist for the 2D tori. The short-period frequency ν_S serves as a suitable stroboscopic mapping frequency as it leads to a shorter total propagation time. Next, the invariant curve is parameterized

with respect to the other angle, θ_M, associated with the medium-period frequency, ν_M. The curve is rendered via Eq. (12), where it must be properly initialized. Of course, the DADM provides suitable starting points. One sample ELFO state in $\bar{\bar{\text{oe}}}$ with $\bar{\bar{a}} = 10,000$ [km], $\bar{\bar{e}} = 0.4082$ [nd], $\bar{\bar{i}} = 45^\circ$, $\bar{\bar{\omega}} = 90^\circ$, $\bar{\bar{\Omega}} = 0^\circ$, and $\bar{\bar{M}} = 180^\circ$, is leveraged in the current section. The transformation process in Fig. 1 is leveraged to supply an initial state within the CR3BP dynamics in the BRF, i.e., $\vec{\rho}, \vec{\rho}'$. Propagating the state for three years supplies the trajectory as plotted in the BRF within Fig. 3(a). Note that the trajectory may deviate from the original initial guess supplied from the DADM. From the shape of the trajectory within the BRF, it is apparent that the z position component is expected to be dominated by the short-period frequency, ν_S, an intuitive result from the fact that $\bar{\bar{\omega}} = 90^\circ$. The DFT on the z position component is plotted in Fig. 3(b) with the nd frequency ν on the horizontal axis and the corresponding amplitude in a $\log_{10}$ scale on the vertical axis, zooming into the lower-frequency domain. Leveraging the frequency collocation algorithm as represented by Eqs. (16)-(18), the refined frequency for ν_S is plotted as the dotted vertical line in Fig. 3(b). With this accurate information for ν_S, the stroboscopic mapping states along the trajectory are generated as black dots near the apolune in Fig. 3(a). Then, the x position components at the stroboscopic map are analyzed with DFT and plotted in Fig. 3(c). As the short-period frequency ν_S is removed via the stroboscopic map, it does not appear within the frequency domain. Then, the most dominant peak is associated with the medium-period frequency ν_M, where the frequency collocation algorithm is leveraged again to retrieve an accurate value. It is notable that secondary peaks appear in the vicinity of ν_M. These peaks correspond to the convoluted frequencies between $\nu_{M,L}$, e.g., $\nu_M \pm \nu_L$. Such long-period frequency oscillations occur as the initial guess supplied by the DADM does not exactly land on the ELFO within the CR3BP; it often locates the nearby 3D tori within the CR3BP. With the goal of constructing a 2D tori within the CR3BP, the invariant curve $\vec{u}(\theta_M)$ in Eq. (12) is constructed by approximating $\boldsymbol{A}$ in Eq. (12). Note that $N_F = 21$ samples are leveraged to approximate the curve. Then, the stroboscopic mapping states (black dots in Fig. 3(a)) serve as approximate data points for $\vec{u}(\theta_M)$. A least-squares solution is determined for the coefficient matrix $\boldsymbol{A}$ that typically serves as a good initial guess to facilitate the convergence to the invariance condition, Eq. (14). One such converged invariant curve is plotted in Fig. 4(a) in the $x - y$ plane along with the stroboscopic mapping states from Fig. 3(a).

3D tori As demonstrated in Fig. 2(c), the 2D tori for the ELFOs are expected to be surrounded by 3D tori. In fact, the sample propagation within Fig. 3(a) indeed locates a nearby 3D tori. Such structures are deliberately constructed leveraging the linear stability information from the 2D tori. As discussed previously, $(6N_F, 6N_F)$ the Jacobian matrix $\boldsymbol{DF}$ contains such information. While the matrix supplies $6N_F$ set of eigenvalues and eigenvectors, Jorba [15] notes that the matrix is *reducible* to a $(6, 6)$ matrix, where the only maximum of 6 unique directions exist. The eigenstructures are identical within each of the 6 groups of N_F elements via rotation. For the 2D tori, $4N_F$ eigenvectors are tangential to the tori and do not contain the information for the nearby 3D tori. The rest, i.e., $2N_F$ eigenvectors, appear to be normal to the 2D tori; any of these eigenvectors may be leveraged to supply initial guess for the nearby 3D tori. One such normal direction is plotted in Fig. 4(b) for the real position components of the eigenvector on top of the invariant curve for the 2D tori. Now, 11 sample points are constructed for θ_L, the angle for the long-period frequency ν_L, at each of the $N_F = 21$ points for θ_M. The state on the invariant curve is then perturbed into the direction that combines the real and imaginary components of the normal eigenvector. Such a linear estimate for the invariant surface is then leveraged to converge to a solution that satisfies the invariance condition. One converged invariant surface from this process is plotted in Fig. 4(c).

Family Continuation and Local Stability Gathering the tools so far, the solution space within the CR3BP is characterized via continuation of 2D and 3D tori in the local vicinity of the desired, nominal ELFO. Assume that the desired solution corresponds to the 2D tori computed in Fig. 4(a). Over multiple years of propagation along this 2D tori, the osculating elements (œ) and the expressions for the integrals of motion are evaluated. Leveraging their average values, the 2D tori are marked as the red star within Fig. 5, visualized within the $C_{Z,H,a}$ space. Starting from this point, different types of 2D and 3D tori families are generated. First, $\sigma_{M,L} = 2\pi\nu_{M,L}/\nu_S$ denote the rotation numbers per stroboscopic period, $T = 2\pi/\nu_S$. The blue and orange markers denote the constant-T and constant-σ_M 2D tori families, respectively. These two directions span the the 2D surface as indicated by the magenta surface in Fig. 5(a), allowing the solution space characterization for the ELFOs in the CR3BP. Caution is required in interpreting Fig. 5, as the values $C_{Z,H,a}$ are no longer constant within the CR3BP; thus, the 2d tori family do not exactly lie on the magenta surface. The nearby structures are navigated via constructing the 3D tori initialized with the linear stability information for the underlying red star 2D tori. Then, while fixing T, σ_M, the σ_L value is varied to generate the 3D tori family.

This process yields several important insights. First, the linear stability of the 2D tori, combined with the explicit construction of 3D tori, suggests superexponential stability within the CR3BP context [23] with dense quasi-periodic orbits. Small perturbations from the reference ELFO result in deviations that grow at a sufficiently slow rate, ensuring practical stability. While the *global* structure of the ELFOs and their surrounding dynamics remains beyond the scope of this investigation, local stability is effectively characterized by continuing 2D and 3D tori near the desired structures for practical applications. Additionally, the tori construction offers a concise representation and systematic search directions for exploring the local solution space, avoiding the inefficiency of less-informed test propagations. The Cartesian state representation in the BRF within the CR3BP also offers valuable insights into geometric changes as a function of frequency evolution. For instance, following the family curves illustrated in Fig. 5 reveals that continuing in the T-fixed, σ_M-direction effectively alters the orbit's eccentricity, as indicated by the orange arrow in Fig. 5(b). This result is intuitive since higher eccentricities experience stronger perturbations from the Earth, leading to faster ν_M values. Similarly, fixing T and σ_M while varying σ_L results in an increase in the invariant surface size relative to the underlying 2D tori. Notably, ν_L decreases from the 2D tori with the ELFO corresponding to a local maximum in ν_L. This behavior is consistent with the observation that the period of trajectories in the $\bar{\bar{e}} - \bar{\bar{\omega}}$ plane (Fig. 2(b)) monotonically increases from the underlying ELFO (★).

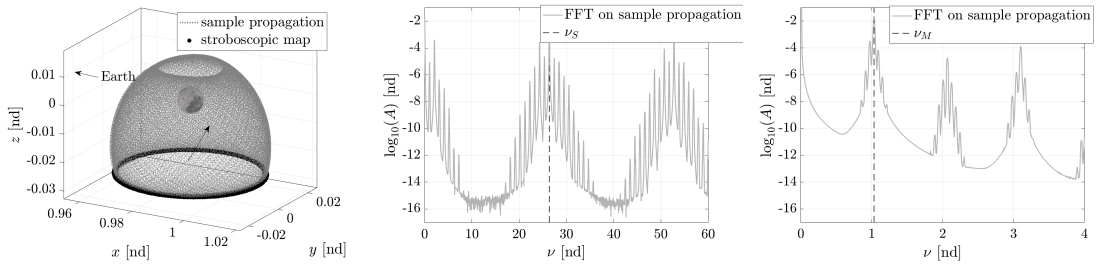

(a) Trajectory over 3 years (b) DFT on z (c) DFT on x at the map

Fig. 3: Initial guess from the DADM, propagated within the CR3BP

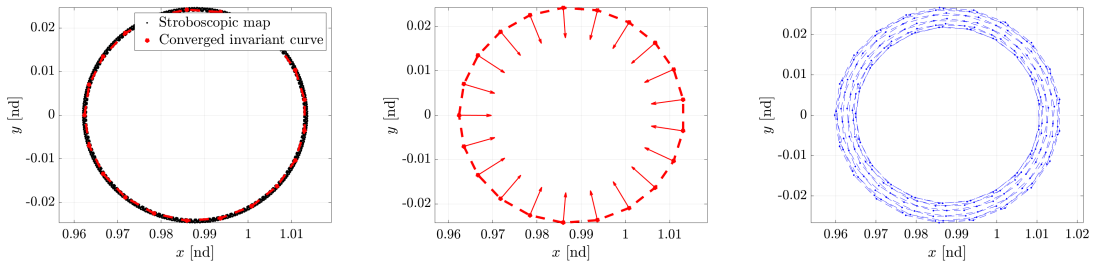

(a) Converged invariant curve (b) Normal eigenvector (c) Converged invariant surface

Fig. 4: Construction of invariant curve and surface within the CR3BP

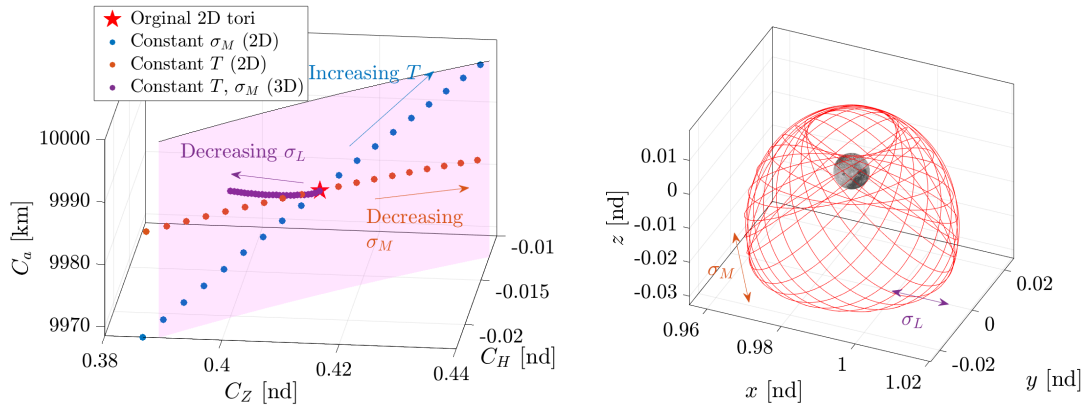

(a) Families of 2D and 3D tori (b) Geometric evolution for $\sigma_{M,L}$

Fig. 5: Families of 2D and 3D tori within the CR3BP

ELFOs in the Higher-Fidelity Ephemeris Model (HFEM)

Even if ELFO solutions exist as dense quasi-periodic structures within the CR3BP, additional perturbations from the HFEM may disrupt these tori. This mechanism of chaos infusion is an active area of research, with resonance being a well-known contributing factor. For instance, medium Earth orbits are prone to long-term instability caused by perturbations from the Moon and Earth oblateness in near-resonance [24, 25]. Similarly, transitioning multi-body structures, such as the Earth-Moon L_2 halo orbit, to higher-fidelity models is challenging due to resonance effects arising from Earth-Moon pulsations [26, 27]. While further research is indeed required to characterize any additional instability within the HFEM, the current study presumes the nominal persistence of the ELFOs and surrounding structures. The 2D and 3D tori from the CR3BP then evolve onto $(2+n)$D and $(3+n)$D tori within the HFEM [28], where the time-dependent perturbations within the HFEM are effectively modeled as n-dimensional quasi-periodic functions [29]. For example, Gómez et al. suggest $n = 5$ for the point-mass HFEM. For such persistence of the ELFOs and surrounding structures as tori, practical stability is ensured even within the HFEM.

Solution Space: Summary

The dimensions of the phase space as well as the solution space involving ELFOs across dynamical models are summarized in Table 1. As discussed previously, however, the table only illustrates a nominal behavior and does not guarantee the persistence of tori across the medium- and higher-fidelity models. Within the CR3BP and HFEM, the ELFOs and nearby structures may track qualitatively different behaviors from the DADM, e.g., the tori may break down due to intersection with hyperbolic manifolds from any multi-body structures, an expected outcome for sufficiently large $\bar{\bar{a}}$. Similarly, certain bifurcations possibly introduce degeneracy in the parameters in describing the evolution of the ELFOs, complicating the simple solution space as illustrated in Fig. 2(c). The nominal case in the current analysis also excludes any resonance between $\nu_{S,M,L}$. In such cases, the dimensions of the tori reduce; for example, ELFOs track periodic orbits within the CR3BP when $\nu_{S,M}$ are in resonance [6, 12].

Table 1: Solution space for the ELFOs and nearby structures across dynamical models

Fidelity	Low	Medium	High
Model name	DADM	CR3BP	HFEM
ELFOs (two-parameter)	2D tori (0D for $\bar{\bar{e}}, \bar{\bar{i}}, \bar{\bar{\omega}}$)	2D tori	(2+n)D tori
Nearby structures (three-parameter)	3D tori (1D for $\bar{\bar{e}}, \bar{\bar{i}}, \bar{\bar{\omega}}$)	3D tori	(3+n)D tori
Phase space dimensionality	6 (3 for $\bar{\bar{e}}, \bar{\bar{i}}, \bar{\bar{\omega}}$)	6	6+n

REFERENCE CONSTELLATION DESIGN IN THE HFEM

Assuming a dense solution space for the ELFOs and nearby structures in the HFEM, it is possible to devise a differential corrector within the frequency domain. This *frequency domain targeter* is introduced, followed by an application in constructing a satellite constellation within the HFEM leveraging the ELFOs and nearby structures satisfying sample mission requirements. While the dynamical model used in this section is the point-mass HFEM, the corrector is inherently model-agnostic, provided the desired solution space is characterized by dense quasi-periodic orbits.

Frequency Domain Targeter

For a six-dimensional initial state $\left[\vec{R}, \vec{R}'\right]$, assuming the trajectory Γ demonstrates a quasi-periodic behavior, a differential corrector is introduced that targets the frequency structure for Γ. Consider a six-dimensional initial state vector $\vec{\mathbb{X}}_0$, consisting of the position and velocity within the JIF, and an initial epoch JD_0, i.e, $\left[\vec{\mathbb{X}}_0, JD_0\right] \in \mathbb{R}^7$. This initial state and epoch map to the frequency structure as follows,

$$\vec{\mathcal{F}}(\vec{\mathbb{X}}_0, JD_0) = \left[\nu_S, \theta_S, \nu_M, \theta_M, \nu_L, \theta_L, \theta_{1-n}\right] \in \mathbb{R}^{6+n}. \tag{26}$$

The first six components exist in three frequency-phase pairs, each associated with the short-, medium-, and long-period frequencies, $\nu_{S,M,L}$. Note that the angles θ_{1-n} are inherited from the initial epoch JD_0 and independent from the initial state vector. The frequencies ν_{1-n} are also automatically inherited from the HFEM dynamics and remain constant; these external model frequencies are

omitted from $\vec{\mathcal{F}}$. For simplicity, in the current analysis, JD_0 is assumed to be fixed. Consequently, adjustments to $\vec{\mathbb{X}}_0$ achieve specific combinations of the first six frequency components. This approach transforms the problem into a root-finding formulation with a six-dimensional guess $\vec{\mathbb{X}}_0$ and a six-dimensional constraint vector defined as,

$$\vec{\mathbb{F}}_{S,M,L}(\vec{\mathbb{X}}_0) = \begin{bmatrix} \nu_{S,M,L} - \nu^*_{S,M,L} \\ \theta_{S,M,L} - \theta^*_{S,M,L} \end{bmatrix}, \tag{27}$$

where the superscript $*$ denotes the target frequency components. For a differential corrector to solve for $\vec{\mathbb{F}} = \vec{0}$, the Jacobian matrix of $\vec{\mathbb{F}}$ with respect to $\vec{\mathbb{X}}_0$ is required, comprising $d\nu_{S,M,L}/d\vec{\mathbb{X}}_0$ and $d\theta_{S,M,L}/d\vec{\mathbb{X}}_0$. Expressions for these sensitivity vectors are derived from Eqs. (16)-(18). Recall that these equations supply refined frequency information (A_i, ν_i, θ_i), with i to be yet decided, given a quasi-periodic signal. Although the equations do not provide explicit solutions for the frequency variables, treating them as implicit equations for A_i, ν_i, θ_i allows differentiation with respect to $\vec{\mathbb{X}}_0$, yielding,

$$\boldsymbol{M}_i \begin{bmatrix} \frac{dA_i}{d\vec{\mathbb{X}}_0} \\ \frac{d\nu_i}{d\vec{\mathbb{X}}_0} \\ \frac{d\theta_i}{d\vec{\mathbb{X}}_0} \end{bmatrix} = \begin{bmatrix} \frac{dc_\Gamma(k)}{d\vec{\mathbb{X}}_0} \\ \frac{ds_\Gamma(k)}{d\vec{\mathbb{X}}_0} \\ \frac{dcs_\Gamma(k\pm1)}{d\vec{\mathbb{X}}_0} \end{bmatrix}, \tag{28}$$

where $\boldsymbol{M}_i$ is a three-by-three invertible matrix with following components,

$$\begin{aligned}
\boldsymbol{M}_i(1,1) &= \cos\theta_i c_{c(\nu_i)}(k) - \sin\theta_i c_{s(\nu_i)}(k) \\
\boldsymbol{M}_i(2,1) &= \cos\theta_i s_{c(\nu_i)}(k) - \sin\theta_i s_{s(\nu_i)}(k) \\
\boldsymbol{M}_i(3,1) &= \cos\theta_i cs_{c(\nu_i)}(k\pm1) - \sin\theta_i cs_{s(\nu_i)}(k\pm1) \\
\boldsymbol{M}_i(1,2) &= -A_i\sin\theta_i c_{c(\nu_i)}(k) - A_i\cos\theta_i c_{s(\nu_i)}(k) \\
\boldsymbol{M}_i(2,2) &= -A_i\sin\theta_i s_{c(\nu_i)}(k) - A_i\cos\theta_i s_{s(\nu_i)}(k) \\
\boldsymbol{M}_i(3,2) &= -A_i\sin\theta_i cs_{c(\nu_i)}(k\pm1) - A_i\cos\theta_i cs_{s(\nu_i)}(k\pm1) \\
\boldsymbol{M}_i(1,3) &= A_i\cos\theta_i \frac{dc_{c(\nu_i)}(k)}{d\nu_i} - A_i\sin\theta_i \frac{dc_{s(\nu_i)}(k)}{d\nu_i} \\
\boldsymbol{M}_i(2,3) &= A_i\cos\theta_i \frac{dc_{c(\nu_i)}(k)}{d\nu_i} - A_i\sin\theta_i \frac{dc_{s(\nu_i)}(k)}{d\nu_i} \\
\boldsymbol{M}_i(3,3) &= A_i\cos\theta_i \frac{dcs_{c(\nu_i)}(k\pm1)}{d\nu_i} - A_i\sin\theta_i \frac{dcs_{s(\nu_i)}(k\pm1)}{d\nu_i}.
\end{aligned} \tag{29}$$

Then, Eq. (28) is solved for $d\nu_i/d\vec{\mathbb{X}}_0, d\theta_i/d\vec{\mathbb{X}}_0$ by inverting the matrix $\boldsymbol{M}_i$. These vectors are in turn leveraged to construct $d\vec{\mathbb{F}}/d\vec{\mathbb{X}}_0$ and iteratively solve for $\vec{\mathbb{F}}(\vec{\mathbb{X}}_0) = \vec{0}$. To implement the frequency domain targeter as described by Eqs. (27)-(29), two additional elements are necessary. Firstly, Eq. (28) is derived from one scalar component of the quasi-periodic signal Γ, requiring the selection of an appropriate component in relevant frames. Secondly, it is crucial to identify specific peaks in the frequency spectrum corresponding to the desired target frequencies, i.e., $\nu_{S,M,L}$. These nuances are detailed for each of the three frequencies.

The Short-Period Frequency, ν_S From the CR3BP analysis in Fig. 4(a), the short-period frequency ν_S is identified as the 1st peak of the Fourier analysis on the z coordinate of the trajectory.

Thus, the right side of Eq. (28) is constructed from Eq. (19) as,

$$\frac{dc_\Gamma(k)}{d\vec{\mathbb{X}}_0} = 2\,\mathrm{Re}\left(\sum_{j=0}^{N-1}\frac{dz(t_j)}{d\vec{\mathbb{X}}_0}h(j)\exp(-2\pi \mathrm{i} jk/N)\right) \tag{30}$$

$$\frac{ds_\Gamma(k)}{d\vec{\mathbb{X}}_0} = -2\,\mathrm{Im}\left(\sum_{j=0}^{N-1}\frac{dz(t_j)}{d\vec{\mathbb{X}}_0}h(j)\exp(-2\pi \mathrm{i} jk/N)\right), \tag{31}$$

with $N = 2^{16}$ to facilitate the Fast Fourier Transform (FFT). The z components are defined within the BRF but $\vec{X}_0$ is propagated within the JIF from Eq. (11). [4] This discrepancy in frames requires a rotation rendered from Eq. (2) as,

$$z(t_j) = \begin{bmatrix}0 & 0 & 1\end{bmatrix}\frac{l_*}{l(t_j)}(\boldsymbol{C}(t_j))^\intercal \vec{R}(t_j) \tag{32}$$

$$\frac{dz(t_j)}{d\vec{\mathbb{X}}_0}\begin{bmatrix}0 & 0 & 1\end{bmatrix}\frac{l_*}{l(t_j)}(\boldsymbol{C}(t_j))^\intercal \frac{d\vec{R}(t_j)}{d\vec{\mathbb{X}}_0} \tag{33}$$

where $\intercal$ is a matrix transpose and a three-by-six matrix $d\vec{R}(t_j)/d\vec{\mathbb{X}}_0$ is trivially retrieved from the state transition matrix following the HFEM dynamics from Eq. (11). Note that the dense nature of the quasi-periodic orbits implies a slow (linear) growth in the norm of the components of the state transition matrix as opposed to an exponential growth with respect to the nd time, t. The matrix $\boldsymbol{M}_i$ from Eq. (29) is constructed with (A_i, ν_i, θ_i) that satisfy Eqs. (16)-(18) with the 1st peak of the DFT on z.

The Medium-Period Frequency, ν_M Detecting relevant peaks from the DFT for the medium- and long-period frequencies is more challenging as they are secondary to the dominant short-period frequency. Identifying $\nu_{M,L}$ is further complicated by the presence of convoluted frequencies between $\nu_{S,M,L}$ and the perturbation-induced frequencies of the HFEM, i.e., ν_{1-n}. To address this complexity, a priori knowledge from the CR3BP analysis is leveraged. For a given initial state $\vec{\mathbb{X}}_0$, the local solution space may be characterized within the CR3BP, providing estimates on the values for $\nu_{M,L}$. Although these values vary across different dynamical models, the estimates from the CR3BP are typically sufficient for identifying the relevant peaks within the HFEM. For example, for the specific local solution space as illustrated in Fig. 5, $\nu_{M,G} \approx 1.034$ [nd] (G for the guess), guiding the selection of peaks in the DFT analysis within the HFEM.

The peaks associated with ν_M generally exhibit smaller magnitudes compared to those of ν_S, rendering the direct refinement with Eqs. (16)-(18) algorithmically unstable. Multiple strategies may be devised to facilitate the detection of the desired frequencies. For example, leveraging the stroboscopic map eliminates the ν_S frequency and enhances the prominence of ν_M as indicated in Fig. 3(c). Another alternative includes targeting a convoluted frequency $\nu_S \pm \nu_M$ that is generally associated with larger amplitudes as opposed to ν_M alone; this option is employed in subsequent sections. Considering the geometry of the quasi-periodic orbits in the BRF (Fig. 5(b)), the x position component (y may be leveraged as well) is leveraged for the DFT analysis, conducive to extracting ν_M. Then, the following procedures are employed: (1) from z position component, ν_S is initially refined from Eqs. (16)-(18), along with the corresponding sensitivity vectors $d\nu_S/d\vec{\mathbb{X}}_0, d\theta_S/d\vec{\mathbb{X}}_0$ from Eq. (28), (2) i-th peak from the DFT analysis that is located closest to $\nu_S \pm \nu_{M,G}$ is identified,

[4] As an alternative, it is possible to leverage the BRF for HFEM propagation, e.g., in [30, 31]

(3) Eqs. (16)-(18) are solved again to supply a refined value ν_M from the i-th peak, and (4) the sensitivity vectors $d\nu_i/d\vec{\mathbb{X}}_0, d\theta_i/d\vec{\mathbb{X}}_0$ are determined from Eq. (28). Note that $d\nu_i/d\vec{\mathbb{X}}_0 = d\nu_S/d\vec{\mathbb{X}}_0 \pm d\nu_M/d\vec{\mathbb{X}}_0$ where the first term on the right side is supplied from the step (1). Similarly, $d\theta_i/d\vec{\mathbb{X}}_0 = d\theta_S/d\vec{\mathbb{X}}_0 \pm d\theta_M/d\vec{\mathbb{X}}_0$.

The Long-Period Frequency, ν_L While detecting and targeting ν_L follows similar steps as those used for ν_M, additional complexities arise. First, for ELFOs tracking 2D tori, the DFT cannot identify oscillations with non-zero amplitudes, as θ_L is poorly defined for these structures. For nearby structures close to the magenta surface in Fig. 2(c), long-period oscillations are associated with small amplitudes. Furthermore, ν_L is obviously associated with a small value, e.g., $\nu_L \approx 0.059$ [nd] for the 3D tori family plotted in Fig. 5. Recall that the resolution of the DFT analysis is limited by $2\pi/t_{N-1}$. To ensure $\nu_L \gg 2\pi/t_{N-1}$ and facilitate detection, the total propagation time must span several decades, potentially leading to significant computational costs. Moreover, during extended propagation, the norm of the state transition matrix from Eq. (32) grows substantially, reducing the robustness of the frequency-targeting process. Note that the long-frequency ν_L governs the deviation from the ELFOs (2D tori), where evolution in ν_L leads to invariant surface spanning wider area as plotted in Figs. 3(c) and 5(b). In light of this observation, in practical applications, controlling the geometric deviation, A_L, may be more desirable than directly targeting ν_L. Note that $A_L = A_L(\nu_S, \nu_M, \nu_L)$. Thus, the constraint vector is well-defined with A_L in lieu of ν_L and serves as an alternative option to supply a square system with a six-dimensional vectors $\vec{\mathbb{X}}_0$ and $\vec{\mathbb{F}}(\vec{\mathbb{X}}_0) = \vec{0}$. With these additional complexities for targeting the long-period frequency ν_L, x position components within the BRF are leveraged to construct Eq. (28).

Overall Process The overall process for ELFO constellation design using the proposed frequency domain targeter, is summarized. The process begins by defining the mission requirements that include nominal operation duration, number of satellites, line-of-sight to specific lunar sites and communications. Based on these requirements, an initial guess for each satellite within the constellation is supplied in terms of $\bar{\bar{\mathfrak{E}}}$. If required, the solution space in the vicinity is explored in the medium-fidelity model, i.e., CR3BP as conducted in Fig. 5. These initial guesses in $\bar{\bar{\mathfrak{E}}}$ are transformed to respective $\vec{\mathbb{X}}_0$ vectors following the schematic in Fig. 1, assuming a fixed initial epoch JD_0. The relative phasing requirements between satellites are encoded into a constraint vector $\vec{\mathbb{F}}$, as defined in Eq. (27). Each satellite in the constellation has a distinct $\vec{\mathbb{F}}$. The state vectors $\vec{\mathbb{X}}_0$ are iteratively adjusted until $\vec{\mathbb{F}} = \vec{0}$. This process leverages Eqs. (16)-(18), (28)-(29), and utilizes appropriate state components, e.g., x, z, to target the short-, medium-, and long-period frequencies. This procedure is repeated for each satellite in the constellation to ensure the entire system meets the desired configuration.

Sample Application: Reference Three-Satellite Constellation Design

The insights and tools developed thus far are demonstrated by generating a reference ELFO constellation of three satellites within the HFEM dynamics. Although specific mission requirements are not detailed here, it is assumed that the desired geometry results in the set of doubly-averaged mean orbital elements ($\bar{\bar{\mathfrak{E}}}$), as illustrated in Table 2, designed to provide coverage of the lunar south pole ($\bar{\bar{\omega}} = 90^\circ$) for approximately 10 years. Phasing requirements are set such that the satellites are separated by 120° in both $\bar{\bar{\Omega}}$ and $\bar{\bar{M}}$, ensuring consistent coverage. While this requirement suggests initial guesses for $\bar{\bar{\mathfrak{E}}}$ offset by 120° in $\bar{\bar{\Omega}}$ and $\bar{\bar{M}}$, the transformed states $\vec{\mathbb{X}}_0$ in the HFEM often fail to meet the desired phasing upon test propagation, requiring adjustments. For the examples presented, the initial epoch is fixed at $JD_0 = 09/23/2024$. The states $\vec{\mathbb{X}}_0$ for the three satellites appear in Table

3. After approximately 10 years of propagation under HFEM dynamics, frequency structures are retrieved using the frequency collocation algorithm (Eqs. (16)-(18)). The resulting trajectories are visualized in Fig. 6(a) leveraging BRF as the reference frame. The plots depict the first ≈ 1.3 days of propagation. Over longer periods, however, phase drift in M and Ω is observed, as apparent in Fig. 6(b). The vertical axis illustrates ΔM and $\Delta\Omega$, the relative phasing between the satellites within the constellation. This phase drift negatively impacts the constellation's ability to maintain consistent coverage and line-of-sight. Table 3 confirms these findings by detailing the frequency structures for ν_S, $\Delta\theta_S$, ν_M, and $\Delta\theta_M$. Here, $\Delta\theta_{S,M}$ are defined as differences relative to Sat 1, with relative phasing information included in parentheses. Arrows indicate whether components overshoot (↑) or undershoot (↓) their desired values. For example, Sat 1 emloys an initial guess $\nu_S = 26.0840$ [nd], while Sat 2 and Sat 3 exhibit slightly higher values (overshot, ↑). The initial design intends for Sat 2 and Sat 3 to lead and lag Sat 1 by 120°, respectively. However, these small deviations in ν_S prevent these satellites from maintaining the desired phase offset, as evident in Fig. 6(b). Similar behavior is observed for ν_M, where the relative configuration for Ω deteriorates over time. Note that $\theta_S \approx \bar{\bar{M}}$ and $\theta_M \approx \bar{\bar{\Omega}}$, although not exactly. Furthermore, the initial phase offsets for ν_S and ν_M deviate slightly from the desired 120° due to limitations in the transformation accuracy described in Fig. 1. For instance, Sat 2 initially leads Sat 1 in θ_S by only 106°, falling short by 14° for the intended offset (undershot ↓).

Utilizing the frequency domain targeter, the state vectors $\vec{\mathbb{X}}_0$ are refined to eliminate the phase drift. The following constraint vector is arbitrarily enforced,

$$\vec{\mathbb{F}} = \begin{bmatrix} \nu_S - 26.1685 \\ \Delta\theta_S - (\pm 120^\circ) \\ \nu_M - 1.0341 \\ \Delta\theta_M - (\pm 120^\circ) \end{bmatrix}. \tag{34}$$

For Sat 1, the angles $\theta_{S,M}$ are not targeted as it is assumed to serve as an arbitrary reference satellite within the constellation. The remaining satellites are adjusted relative to Sat 1 with phase offsets of $\pm 120^\circ$. The long-period frequency component, ν_L, is not explicitly targeted. Instead, it is assumed that the quasi-periodic oscillation magnitude in x associated with $\nu_L \approx 0.059$ [nd] is desired to be capped at $1 \cdot 10^{-6}$ [nd]. Solving Eq. (34) using a minimum-norm approach ensures that $A_{x,L}$ (the oscillation magnitude in x) does not significantly deviate from its original value; while $A_{x,L}$ is monitored, it is not explicitly constrained in this example. The resulting state vectors $\vec{\mathbb{X}}_0$ are provided in Table 3. The frequency structures are now fully targeted successfully, as indicated by green check marks (✓). The targeted frequencies ν_S and ν_M match within a tolerance of $1 \cdot 10^{-7}$ [nd], and the initial phase angles are set to be 120° apart with a tolerance of $1 \cdot 10^{-7}$ radians. This information is confirmed by examining the evolution of relative M, Ω angles over ≈ 10 years as plotted in Fig. 7(b). While the oscillations exist due to the nature of the osculating elements (œ), it is obvious that the relative phasing across the constellation remains stable, ensuring consistent performance.

Table 2: Set of doubly-averaged mean orbital elements for the three-satellite constellation

$\bar{\bar{\text{œ}}}$	$\bar{\bar{a}}$	$\bar{\bar{e}}$	$\bar{\bar{i}}$	$\bar{\bar{\Omega}}$	$\bar{\bar{\omega}}$	$\bar{\bar{M}}$
Value	$10,000$ [km]	0.4082 [nd]	45°	$0^\circ, 120^\circ, 240^\circ$	90°	$180^\circ, 300^\circ, 60^\circ$

Table 3: Constellation constructed on 09/23/2024 (✓: targeted, ↑: overshoot, ↓: undershoot) [5]

	Initial guess			Targeted and converged		
Sat No.	Sat 1	Sat 2	Sat 3	Sat 1	Sat 2	Sat 3
ν_S [nd]	26.0840 (N/A)	26.1687 (↑0.09)	26.1685 (↑0.09)	26.1685 (N/A)	26.1685 (✓)	26.1685 (✓)
$\Delta\theta_S$ [deg]	0° (N/A)	106° (↓14°)	242° (↑2°)	0° (N/A)	120° (✓)	240° (✓)
ν_M [nd]	1.0341 (N/A)	1.0367 (↑0.026)	1.0327 (↓0.014)	1.0341 (N/A)	1.0341 (✓)	1.0341 (✓)
$\Delta\theta_M$ [deg]	0° (N/A)	133° (↑13°)	235° (↓5°)	0° (N/A)	120° (✓)	240° (✓)
$A_{x,L}$ [nd]	$< 1 \cdot 10^{-6}$	$< 1 \cdot 10^{-6}$	$< 1 \cdot 10^{-6}$	$< 1 \cdot 10^{-6}$	$< 1 \cdot 10^{-6}$	$< 1 \cdot 10^{-6}$
X [nd]	$2.3681 \cdot 10^{-2}$	$-2.4116 \cdot 10^{-2}$	$-1.8681 \cdot 10^{-2}$	$2.3046 \cdot 10^{-2}$	$-2.4121 \cdot 10^{-2}$	$-1.8170 \cdot 10^{-2}$
Y [nd]	$3.9275 \cdot 10^{-3}$	$4.3168 \cdot 10^{-3}$	$1.5963 \cdot 10^{-2}$	$4.5786 \cdot 10^{-3}$	$4.4484 \cdot 10^{-3}$	$1.6671 \cdot 10^{-2}$
Z [nd]	$-2.7631 \cdot 10^{-2}$	$-3.4412 \cdot 10^{-3}$	$2.8722 \cdot 10^{-3}$	$-2.7283 \cdot 10^{-2}$	$-2.4864 \cdot 10^{-3}$	$2.5967 \cdot 10^{-3}$
X' [nd]	$1.6878 \cdot 10^{-1}$	$1.4913 \cdot 10^{-1}$	$-4.5236 \cdot 10^{-1}$	$1.7087 \cdot 10^{-1}$	$1.5159 \cdot 10^{-1}$	$-4.4563 \cdot 10^{-1}$
Y' [nd]	$3.6168 \cdot 10^{-1}$	$-6.7205 \cdot 10^{-1}$	$2.2267 \cdot 10^{-2}$	$3.7412 \cdot 10^{-1}$	$-6.7573 \cdot 10^{-1}$	$2.5913 \cdot 10^{-2}$
Z' [nd]	$1.9606 \cdot 10^{-1}$	$2.0540 \cdot 10^{-1}$	$-5.5763 \cdot 10^{-1}$	$1.9643 \cdot 10^{-1}$	$1.9973 \cdot 10^{-1}$	$-5.6094 \cdot 10^{-1}$

Advantages of the Proposed Strategy

The proposed strategy that leverages the dense nature of the ELFO solution space and frequency domain targeter provides multiple benefits in constellation design and operation. While manually adjusting the initial guesses provided by the DADM can achieve a desired constellation, the current approach offers a scalable, automatable scheme to reference constellation design. The frequency domain constraints are seamlessly integrated with other mission requirements, enabling a systematic search for optimal constellations. This strategy also delivers precise control over all six frequency coordinates, a task that is difficult to accomplish through manual orbital element adjustments. For example, although the semi-major axis ($\bar{\bar{a}}$ or a) primarily influences ν_S, all orbital elements collectively affect the frequency structure. Similarly, achieving a phase separation of 120° among three satellites is not naturally achievable through orbital element adjustments alone. Instead, this technique directly and accurately targets such configurations. Although this investigation

[5] The angles $\Delta\theta_S$, $\Delta\theta_M$ are defined with respect to Sat 1.

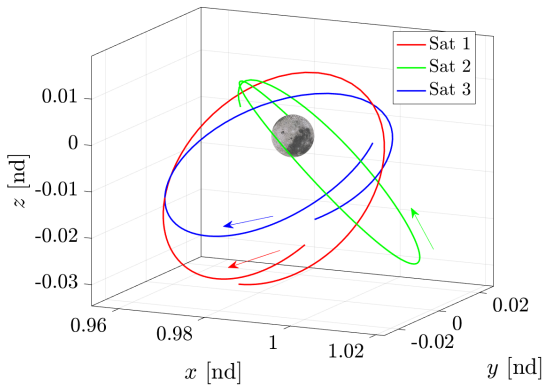

(a) Trajectories for the first ≈ 1.3 days

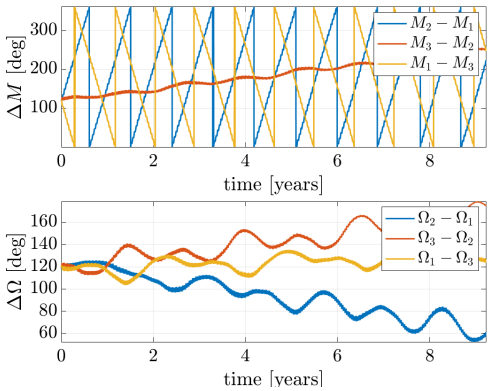

(b) Phase drift in M, Ω[6]

Fig. 6: Initial guess for the three-satellite constellation

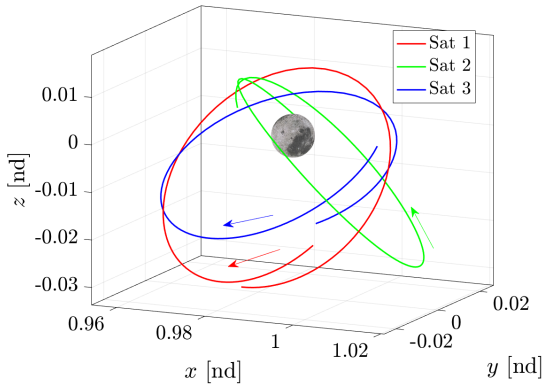

(a) Trajectories for the first ≈ 1.3 days

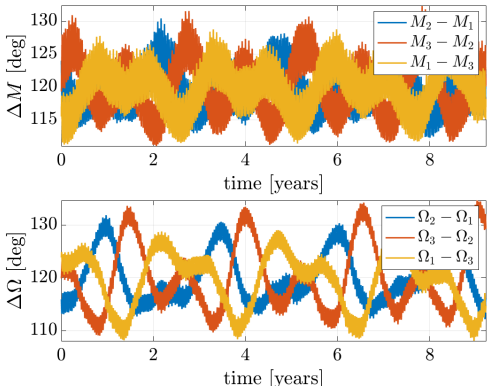

(b) Phase drift in M, Ω

Fig. 7: Targeted and converged three-satellite constellation

focuses on reference constellation design, the Jacobian matrix $d\vec{\mathbb{F}}/d\vec{\mathbb{X}}_0$ and its inverse provide valuable operational insights. For example, the impact of stochastic errors in the spacecraft state on downstream phasing information is linearly predicted using the matrix $d\vec{\mathbb{F}}/d\vec{\mathbb{X}}_0$. This predictive capability enhances operational robustness. Finally, the proposed methodology is agnostic to specific models and frame representations, enabling a versatile and general-purpose mission design tool for ELFOs.

CONCLUDING REMARKS

A satellite constellation design strategy leveraging the Elliptical Lunar Frozen Orbits (ELFOs) is proposed. Various dynamical models for evolving fidelity are utilized to illustrate the characteristics of ELFOs and the surrounding structures. The existence of *dense* quasi-periodic orbits within the

[6]Note that the desired phase drift values for M, Ω are 120° on average. The subscripts $1, 2, 3$ denote Sat 1, 2, 3; for example, $M_2 - M_1$ corresponds to the phase difference between Sat 2 with respect to Sat 1. The same description applies to Fig. 7(b) as well.

Circular Restricted Three-Body Problem (CR3BP) is demonstrated, serving as an intermediate model that bridges the gap between the lower-fidelity Doubly-Averaged Dynamical Model (DADM) and the high-fidelity Higher-Fidelity Ephemeris Model (HFEM). Leveraging this dense quasi-periodic solution space, a frequency domain targeter is developed to refine initial guesses for satellites forming a lunar constellation within the ELFOs. The method enables precise targeting of different frequency components within designated tolerances, ensuring that the desired coverage and phasing requirements are met for a specified mission timeline.

ACKNOWLEDGEMENTS

Valuable discussions with members from Multi-Body Dynamics Research Group are appreciated. Portions of this work were completed at Purdue University under Intuitive Machines LLC Award 21123283.

REFERENCES

[1] B. Baker-McEvilly, S. Bhadauria, D. Canales, and C. Frueh, "A comprehensive review on Cis-lunar expansion and space domain awareness," *Progress in Aerospace Sciences*, Vol. 147, 2024, doi:10.1016/j.paerosci.2024.101019.

[2] T. Nie and P. Gurfil, "Lunar frozen orbits revisited," *Celestial Mechanics and Dynamical Astronomy*, Vol. 130, No. 10, 2018, doi:10.1007/s10569-018-9858-0.

[3] T. A. Ely, "Stable constellations of frozen elliptical inclined lunar orbits," *the Journal of the Astronautical Sciences*, Vol. 53, 2005, doi:10.1007/BF03546355.

[4] D. Folta and D. Quinn, "Lunar frozen orbits," *AIAA/AAS Astrodynamics Specialist Conference and Exhibit*, 2006, p. 6749.

[5] A. F. B. Almeida Prado, "Third-body perturbation in orbits around natural satellites," *Journal of Guidance, Control, and Dynamics*, Vol. 26, No. 1, 2003, doi:10.2514/2.5042.

[6] K. Howell, D. Grebow, and Z. Olikara, "Design using Gauss' perturbing equations with applications to lunar south pole coverage," *Adv. Astronaut. Sci*, Vol. 127, 2007,

[7] T. A. Ely and E. Lieb, "Constellations of elliptical inclined lunar orbits providing polar and global coverage," *the Journal of the Astronautical Sciences*, Vol. 54, No. 1, 2006, doi:10.1007/BF03256476.

[8] R. A. Broucke, "Long-term third-body effects via double averaging," *Journal of Guidance, Control, and Dynamics*, Vol. 26, No. 1, 2003, doi:10.2514/2.5041.

[9] D. A. Vallado, *Fundamentals of astrodynamics and applications*, Vol. 12. Springer Science & Business Media,

[10] R. S. Park, W. M. Folkner, J. G. Williams, and D. H. Boggs, "The JPL planetary and lunar ephemerides DE440 and DE441," *The Astronomical Journal*, Vol. 161, No. 3, 2021, doi:10.3847/1538-3881/abd414.

[11] J. M. Longuski, F. R. Hoots, and G. E. Pollock IV, *Introduction to Orbital Perturbations*, Vol. 40. Springer Nature,

[12] S. McArdle and R. P. Russell, "Circulating, eccentric periodic orbits at the Moon," *Celestial Mechanics and Dynamical Astronomy*, Vol. 133, 2021, doi:10.1007/s10569-021-10013-z.

[13] G. Gómez and J. Mondelo, "The dynamics around the collinear equilibrium points of the RTBP," *Physica D: Nonlinear Phenomena*, Vol. 157, No. 4, 2001, doi:10.1016/S0167-2789(01)00312-8.

[14] Z. P. Olikara and D. J. Scheeres, "Numerical method for computing quasi-periodic orbits and their stability in the restricted three-body problem," *Advances in the Astronautical Sciences*, Vol. 145, No. 911-930, 2012,

[15] À. Jorba, "Numerical computation of the normal behaviour of invariant curves of n-dimensional maps," *Nonlinearity*, Vol. 14, No. 5, 2001, doi:10.1088/0951-7715/14/5/303.

[16] N. Baresi and D. J. Scheeres, "Quasi-periodic invariant tori of time-periodic dynamical systems: Applications to small body exploration," *Proceedings of the International Astronautical Congress*, International Astronautical Federation Paris, France, 2016, pp. 9–26.

[17] B. Park, R. R. Sanaga, and K. C. Howell, "Bridging Ephemeris Transition Gaps: Quasi-Periodic Extensions for the Hill Restricted Four-Body Problem in Cislunar Space," *Proceedings of the International Astronautical Congress*, International Astronautical Federation Milan, Italy, 2024, pp. 9–26.

[18] G. Gómez, J.-M. Mondelo, and C. Simó, "A collocation method for the numerical Fourier analysis of quasi-periodic functions. I. Numerical tests and examples," *Discrete Contin. Dyn. Syst. Ser. B*, Vol. 14, No. 1, 2010, doi:10.3934/dcdsb.2010.14.41.

[19] R. G. Lyons, *Understanding digital signal processing, 3/E*. Pearson,

[20] G. Gómez, J.-M. Mondelo, and C. Simó, "A collocation method for the numerical Fourier analysis of quasi-periodic functions. II. Analytical error estimates," *Discrete Contin. Dyn. Syst. Ser. B*, Vol. 14, No. 1, 2010, doi:10.3934/dcdsb.2010.14.75.

[21] V. I. Arnold, *Mathematical methods of classical mechanics*, Vol. 60. Springer Science & Business Media,

[22] A. Celletti, "From infinite to finite time stability in Celestial Mechanics and Astrodynamics," *Astrophysics and Space Science*, Vol. 368, No. 12, 2023, doi:10.1007/s10509-023-04264-5.

[23] A. Morbidelli and A. Giorgilli, "Superexponential stability of KAM tori," *Journal of statistical physics*, Vol. 78, 1995, doi:10.1007/BF02180145.

[24] J. Daquin, A. J. Rosengren, E. M. Alessi, F. Deleflie, G. B. Valsecchi, and A. Rossi, "The dynamical structure of the MEO region: long-term stability, chaos, and transport," *Celestial Mechanics and Dynamical Astronomy*, Vol. 124, 2016, doi:10.1007/s10569-015-9665-9.

[25] A. J. Rosengren, E. M. Alessi, A. Rossi, and G. B. Valsecchi, "Chaos in navigation satellite orbits caused by the perturbed motion of the Moon," *Monthly Notices of the Royal Astronomical Society*, Vol. 449, No. 4, 2015, doi:10.1093/mnras/stv534.

[26] B. Park and K. Howell, "Characterizing Transition-Challenging Regions Leveraging the Elliptic Restricted Three-Body Problem: L2 Halo Orbits," *AIAA SCITECH 2024 Forum*, 2024, p. 1455.

[27] R. R. Sanaga and K. Howell, "Analyzing the Challenging Region in the Earth-Moon L2 Halo Family via Hill Restricted Four-Body Problem Dynamics," *AIAA SCITECH 2024 Forum*, 2024, p. 1451.

[28] A. Jorba and J. Villanueva, "On the persistence of lower dimensional invariant tori under quasi-periodic perturbations," *Journal of Nonlinear Science*, Vol. 7, 1997, doi:10.1007/s003329900036.

[29] G. Gómez, J. J. Masdemont, and J.-M. Mondelo, "Solar system models with a selected set of frequencies," *Astronomy & Astrophysics*, Vol. 390, No. 2, 2002, doi:10.1051/0004-6361:20020625.

[30] D. A. Dei Tos and F. Topputo, "Trajectory refinement of three-body orbits in the real solar system model," *Advances in Space Research*, Vol. 59, No. 8, 2017, doi:10.1016/j.asr.2017.01.039.

[31] R. R. Sanaga, B. Park, and K. C. Howell, "A Unified Numerical Transition Scheme between dynamical models within cislunar space," *AAS/AIAA Space Flight Mechanics Meeting, Kauai, Hawaii, January 19-23*, 2025.